PHYSICAL REVIEW C VOLUME 25, NUMBER 1 JANUARY 1982

$^{165}Ho + {}^{56}Fe$ reaction at $E_{lab} = 462$ MeV

A. D. Hoover,* J. R. Birkelund, D. Hilscher,† W. U. Schröder, W. W. Wilcke, and J. R. Huizenga
Departments of Chemistry and Physics and Nuclear Structure Research Laboratory, University of Rochester, Rochester, New York 14627

H. Breuer and A. C. Mignerey
Departments of Chemistry and Physics, University of Maryland, College Park, Maryland 20742

V. E. Viola, Jr.
Department of Chemistry, Indiana University, Bloomington, Indiana 47405

K. L. Wolf
Argonne National Laboratory, Argonne, Illinois 60439
(Received 24 July 1981)

The system $^{165}Ho + {}^{56}Fe$ was studied at a bombarding energy of $E_{lab} = 462$ MeV. The experimental Z distributions measured as a function of angle and energy are discussed. The integrated fragment Z distribution of the light reaction fragment is fairly broad and centered close to the charge of the projectile. The kinetic energy distribution extends from the quasielastic region down to energies smaller than the Coulomb energy of touching spherical nuclei. The angular distribution is peaked forward of the quarter-point angle and rises at small angles, which is interpreted as due to orbiting. Correlations of observed fragment Z distributions with energy loss give an indication of the progress of the reaction. Charge distributions show an average drift towards larger asymmetry and an increase in width with increasing energy damping. Results are presented taking account of the Coulomb barrier for two choices of the scission radius. With the aid of a phenomenological description, the initial angular momenta l_i and interaction times are deduced. Interaction times are compared to other characteristic times for the reaction as a function of l. Results from a classical dynamical model using a proximity formalism and one-body transport are shown for comparison to experimental observables and deduced quantities. The influence of a neck degree of freedom on the calculated trajectories is studied in some detail.

[NUCLEAR REACTIONS $^{165}Ho(^{56}Fe,x)$, $E_{lab} = 462$ MeV; measured $\sigma(\theta,E,Z)$; damped reaction; fusion-fusion; deduced angular momenta, interaction times; comparison to dynamical calculations.]

I. INTRODUCTION

Heavy-ion reaction phenomena at bombarding energies several MeV/nucleon above the Coulomb barrier have been studied[1] in order to gain an understanding of the intricate mechanisms involved. The $^{165}Ho + {}^{56}Fe$ system is a projectile/target combination which enables the study of all facets of heavy-ion reaction mechanisms, ranging from elastic scattering to fusion-fission. During the past few years, an effort has been made to investigate systematically all aspects of this reaction. Thus far, measurements of neutron emission,[2] the fusion-fission excitation function,[3] and charge and mass equilibration[4] have been reported. Studies of charged-particle emission[5] in the reaction are currently in progress. The present work emphasizes the measurements and interpretations of projectilelike fragment Z distributions and their dependence on energy loss and scattering angle for the damped (deep inelastic) component.

In the following, the damped reaction will be discussed in some detail. Section II is concerned with the experimental and data analysis pro-

cedures. Measured charge, energy, and angular distributions are described in Sec. III and phenomenological and microscopic interpretations of the reaction are presented in Secs. IV and V, respectively. Conclusions are drawn in Sec. VI.

II. EXPERIMENTAL PROCEDURE AND DATA ANALYSIS

A 435 μg/cm^2 self-supporting ^{165}Ho target was bombarded with a 462-MeV ^{56}Fe beam supplied by the Lawrence Berkeley Laboratory SuperHILAC accelerator. Reaction products were detected at various angles using silicon surface barrier detectors. Two ΔE-E telescopes were used, consisting of transmission detectors of 15.9 and 9.4 μm thicknesses, and stop detectors of 100 μm thickness. The latter telescope was placed at backward angles primarily for charge identification of the low energy, more highly damped, and fusion-fission events. Two monitor detectors were situated above the reaction plane, on either side of the beam, at a total scattering angle of 18° for the determination of the beam intensity and dead time of the data acquisition system. Each telescope was protected by a 0.13 μm thick nickel foil and rare-earth magnets, used to deflect δ electrons produced in the target. The energy calibration was made with ^{252}Cf fission, ^{148}Gd, and ThC alpha sources, the latter two being used for normalization of a precision pulse generator. Energy resolution achieved for elastically scattered projectiles was about 3% (FWHM). Resolution in atomic number was better than 0.8 unit in the interesting range of Z values at and below Z=27.

A standard electronics setup was used, as described in Ref. 6. The dead time of the data acquisition system ranged from 5–20%. Data were recorded event by event on magnetic tape for off-line analysis.

As an example of raw data, the laboratory kinetic energy spectra are plotted in Fig. 1 for four different laboratory angles. In order to concentrate on the damped part of the distributions, the fusion-fission events have been eliminated from the spectra. At the most forward angles shown, the spectra are dominated by an intense elastic scattering peak. Quasielastic events broaden this peak at larger angles. At θ_{lab}=16° and 20° two broad low-energy peaks are observable. The lower-energy peak is suggestive of an orbiting mechanism, where the intermediate dinuclear system rotates for a period of time long enough for damped fragments

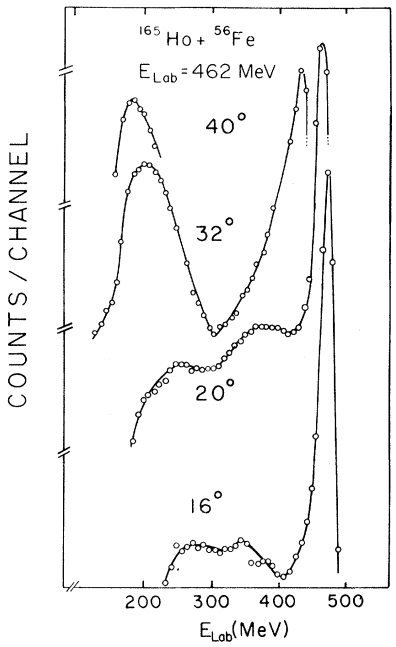

FIG. 1. Laboratory energy spectra of damped fragments from the ^{165}Ho + ^{56}Fe reaction for a beam energy of 462 MeV at the angles indicated, plotted in a linear scale.

to reach negative scattering angles. Its difference in energy from the partially damped peak increases with angle until it begins to dominate the spectra as the scattering angle is increased beyond the quarter-point angle, $\theta_{1/4}$(lab)=32.5°.

As observed in Fig. 1, quasielastic events are difficult to separate from elastic events near the grazing angle. Singles energy spectra from both telescopes were examined in order to obtain elastic scattering angular distributions and to determine the reaction cross section. Standard elastic peak shapes defined at forward angles were used to fit spectra at more backward angles in order to obtain the elastic scattering cross section. This procedure is described in detail in Ref. 7. At small angles, slit-scattering events present in the region defined by the projectile were estimated and removed.

In order to convert the ΔE-E distributions to a Z-E scale, the stopping powers of argon, iron, krypton, and xenon projectiles were measured as a function of energy. The same detector systems were maintained throughout the measurements. A 300 μg/cm^2 bismuth target was used in the iron and argon beam experiments. Energy loss calibration curves were constructed from the positions of the elastic peaks which were varied in energy by inserting 130–420 μm Al degrader foils into the

beam.

Conventional methods for obtaining a Z conversion compare experimental stopping powers with tabulated values. However, stopping power curves derived from range tables of Northcliffe and Schilling[8] did not provide a satisfactory fit to the experimental results. More recent calculations by Hubert *et al.*[9] agree more closely with the data; however, they cover a limited range in energy and became available only after completion of the present analysis. The experimental stopping power curves were fitted with a smooth composite function of the form

$$\frac{\Delta E}{\Delta x} = \begin{cases} x/(ax^2+bx+c), & x < x_0 , \\ a'x^2+b'x+c', & x \geq x_0 , \end{cases} \tag{2.1}$$

where $x = E/A$ and x_0 is close to the energy of the Bragg maximum. The six constants were derived from the maximum energy loss, continuity at x_0, and the value of the function at $E/A = 9$ MeV/nucleon. The relative values of the energy loss for fragments other than argon, iron, krypton, and xenon were obtained from the interpolation of these fits. A mass to charge ratio of 2.15, equivalent to that of the projectile, was used for the fragments in the conversion procedure. All Z conversions were performed event by event so that the resolution in Z would be preserved.

Prior to conversion to the center-of-mass system, fusion-fission events were subtracted from the experimental distributions. Since at many angles the distinction between events from different reaction types was not clear cut, the method used involved some arbitrariness. An upper limit of $Z=35$ was assumed for the damped events, a value corresponding approximately to an intensity minimum separating the fusion-fission and damped events. However, for the determination of the fusion-fission cross section, the area corresponding to fusion-fission events was integrated directly from ΔE-E spectra at angles where the separation was unambiguous, making no arbitrary constraint on the fragment charge.

A number of corrections were made to the measured fragment energies in order to determine the final kinetic energy in the center-of-mass frame of reference. Pulse-height defect corrections were made using the procedure of Kaufman *et al.*[10] A more recent paper by Moulton *et al.*[11] predicts pulse-height defects for the damped products which are larger, but well within the range of the error for this experiment. A correction was also made to account for the energy loss in the nickel foils placed in front of the detectors. These two corrections were small, ranging from 4–9 MeV.

A more significant correction was made during the center-of-mass transformation to account for the neutrons evaporated from the fragments after the primary reaction. The emission of neutrons from a primary fragment leads to a reduction of the fragment kinetic energies and a broadening of the energy distribution. Each emitted neutron is assumed to reduce the fragment excitation energy by 12 MeV, an assumption supported by experiment.[2] The total energy loss was calculated as the difference between the initial kinetic energy and the mean kinetic energy prior to neutron emission. Possible charged-particle emission during the interaction was not accounted for in the analysis; however, such contributions were estimated from evaporation calculations and are discussed in Sec. V B.

Data transformed into the center of mass were then stored in three-dimensional arrays (Z,θ,E) for further manipulation. Various projections and distributions of these data will be discussed in subsequent sections of this paper.

III. RESULTS AND DISCUSSION

A. Elastic scattering

Elastic scattering of ^{56}Fe on ^{165}Ho was studied to determine the quarter-point angle $\theta_{1/4}$, the strong-absorption radius, the total reaction cross section, and the grazing angular momentum. The elastic scattering angular distribution is shown in Fig. 2 as the ratio $d\sigma_{\rm el}/d\sigma_{\rm Ruth}$ of elastic to Rutherford cross section. For center-of-mass angles less than about 35° Coulomb scattering predominates. The sharp falloff of the distribution from unity at larger angles indicates the sudden onset of nuclear interactions.

Two theoretical models were used to analyze the elastically scattered cross sections: the Fresnel model and an optical model. The reaction parameters deduced are summarized in Table I. The optical model utilizes a nuclear interaction potential of the Woods-Saxon form dependent upon the radial separation of the two ions. The solid line in Fig. 2 refers to a four parameter fit using the computer code GENOA,[12] where the real and imaginary surface diffusenesses, $a_R = a_I = 0.529$ fm, were kept constant and the radii varied. The Coulomb potential was approximated by the potential between a

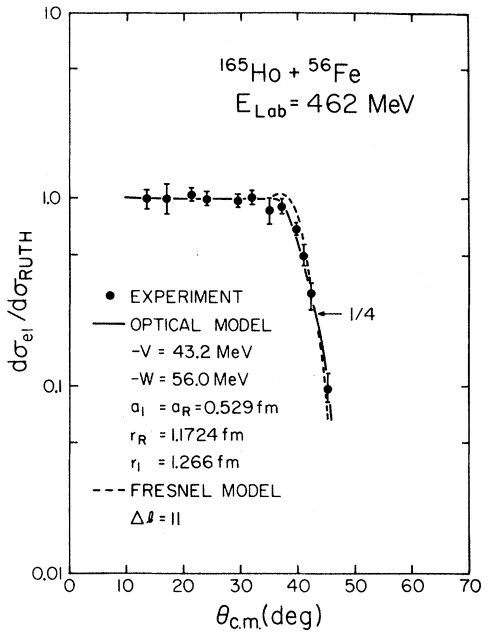

FIG. 2. The experimental ratio $d\sigma_{el}/d\sigma_{Ruth}$ of the elastic to Rutherford cross section is given as a function of center-of-mass scattering angle and is compared to calculations using the generalized Fresnel model (dashed curve) and the optical model (solid curve).

TABLE I. Reaction parameters for the system ^{165}Ho + ^{56}Fe at E_{lab}=462 MeV.

E_{lab}	(462±14) MeV
$E_{c.m.}$	(345±10) MeV
$\theta_{1/4}$(lab)	32.5°±0.4°
$\theta_{1/4}$(c.m.)	43.0°±0.5°
μ (reduced mass)	41.8 u
k_∞ (wave number)	26.27 fm^{-1}
η (Coulomb parameter)	95.50
R_{int} (Fresnel)	(13.6±0.1) fm
l_g (Fresnel exp $\theta_{1/4}$)	(242±3)$\hbar$
σ_R (Fresnel exp $\theta_{1/4}$)	(2.94±0.24) b
σ_R (exp)	$(3.3^{+0.2}_{-0.8})$ b
R_{SA} (optical model)	(13.5±0.1) fm
l_{max} (optical model)	(239±3)$\hbar$
σ_R (optical model)	(2.94±0.10) b
$V_C(R_{SA})$	185 MeV
$E_0=E_{c.m.}-V_C(R_{SA})$	160 MeV
$[E_{c.m.}-V_C(R_{SA})]/\mu$	3.83 MeV/nucleon
$\sigma_{fusion-fission}$ (exp)	(0.72±0.10) b
l_{crit}	(125±9)$\hbar$
l_{RLDM}	66$\hbar$

point charge and a uniformly charged sphere, with radius $R_C=0.75(A_T^{1/3}+A_P^{1/3})$. The deduced radii and depths of the real and imaginary potentials were $r_R=1.172$ fm, $r_I=1.266$ fm, $-V=43.2$ MeV, and $-W=56.0$ MeV, respectively. This particular fit is representative of several good fits that can be made to the data by modifying the different parameters simultaneously. The maximum angular momentum leading to a reaction was deduced to be $l_{max}=239\hbar$, the value corresponding to a transmission coefficient $T_l=\frac{3}{4}$. The strong-absorption radius as defined for a Coulomb trajectory is

$$R_{SA}=\frac{1}{k}\{\eta+[\eta^2+l_{max}(l_{max}+1)]^{1/2}\}\ , \quad (3.1)$$

where η is the Sommerfeld parameter and k is the inverse wave number. The optical model calculations yielded $R_{SA}=13.45$ fm and a reaction cross section $\sigma_R=(2.94\pm0.10)$ b.

The Fresnel model[13] assumes a transmission coefficient of $T_l=1$ for l waves up to a grazing angular momentum l_g, and $T_l=0$ for larger l waves. In a generalized version of this model, Frahn[14] incorporates a gradual transition in angular momentum space where the transmission coefficient varies smoothly from 0 to 1, with the condition that $T_l=\frac{3}{4}$ at $l=l_g$. The total reaction cross section is then expressed as

$$\sigma_R=\pi\lambda\!\!\!^{-2}(l_g+\tfrac{1}{2})^2\left[1+2\frac{\Delta l}{l_g+\frac{1}{2}}+\frac{\pi^2}{3}\left[\frac{\Delta l}{l_g+\frac{1}{2}}\right]^2\right], \quad (3.2)$$

where Δl is the width of the region in angular momentum where the transmission coefficient changes from 0 to 1. The interaction radius is given as

$$R_{int}=r_0(A_P^{1/3}+A_T^{1/3}) =\frac{\eta}{k}[1+\csc(\tfrac{1}{2}\theta_{1/4})]\ . \quad (3.3)$$

The Fresnel model calculation with $\Delta l=11\hbar$ is represented by a dashed line in Fig. 2. Similar calculations were made with values of Δl ranging from 5 to 10 which, for the most part, lead to a variation in the amplitude of the oscillations appearing in the forward region of the theoretical elastic scattering angular distribution. In the results shown Δl corresponds to the 90−10% range of transmission coefficients as calculated by the optical model. The parameters determined by this Fresnel calculation were $l_g=242\hbar$, $R_{int}=13.56$ fm, and $\sigma_R=(2.94\pm0.24)$ b, in good agreement with

the optical model analysis. However, due to the poor energy resolution in this experiment, it is important to point out that the data of Fig. 2 contain contributions from inelastic processes in an amount that is difficult to estimate. Hence, the total reaction cross section may be larger than the above one extracted from an analysis of the "elastic" scattering data of Fig. 2.

B. Damped reactions

The laboratory angular distribution of the damped component of the reaction cross section defined by the reaction products excluding fusion-fission fragments is shown in Fig. 3. A strong focusing of the distribution is visible, with a quasielastic peak slightly forward of the quarter-point angle $\theta_{1/4}(\text{lab})=32.5°$. At the most forward angles the cross section rises sharply, a phenomenon which may be attributed to orbiting, i.e., scattering to negative angles. Since it was not experimentally feasible to extend the measurement to angles less than 10°, the curve through the data in Fig. 3 was extrapolated linearly to zero degrees, for purposes of determining the damped cross section. The region from 0°—10° corresponded to approximately 15% of the damped cross section. The cross section for the damped events was $\sigma_d=(2.6\pm0.6)$ b, whereas the total reaction cross section, determined from direct integration of reaction events, including the fusion-fission component, was $\sigma_R=(3.3^{+0.2}_{-0.8})$ b, in reasonable agreement with the values deduced from the elastic scattering analyses.

Figure 4 shows the charge distribution of the light reaction fragments integrated over energy and angle. Of note in this figure is the large number of fragments with atomic numbers below that of the projectile. In fact, the maximum of the overall cross section is centered below $Z=26$, a subject to be discussed in more detail in Sec. III C. The enhanced cross section observed at higher Z values is due to the onset of fusion-fission and more highly damped events.

The energy distribution of the damped events is shown in Fig. 5. The peak at low energy losses represents quasielastic processes, whereas damped reactions comprise the broad peak at higher energy losses. The dashed part of the distribution represents a cross section of 100 mb associated with events where the total final kinetic energy was less than 125 MeV, below the threshold of this experiment. Reactions leading to fragments at far backward angles also contribute to the missing cross section. A substantial amount of cross section is associated with final energies less than the Coulomb energies of touching spheres signifying large deformations of the intermediate complex at scission. The arrow in Fig. 5 denotes the available kinetic energy in the entrance channel, $E_{\text{c.m.}}-V_C(R_{\text{SA}})$.

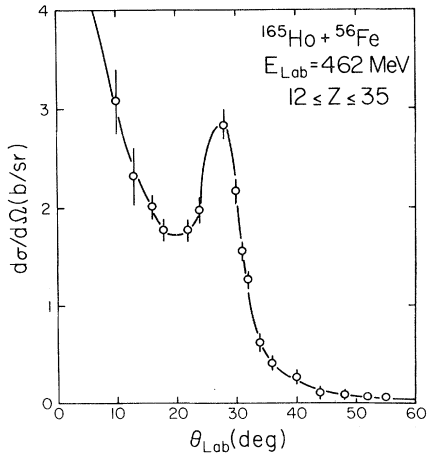

FIG. 3. The angular distribution in the laboratory frame for the Fe-like products, excluding fusion-fission events. The solid line serves to guide the eye.

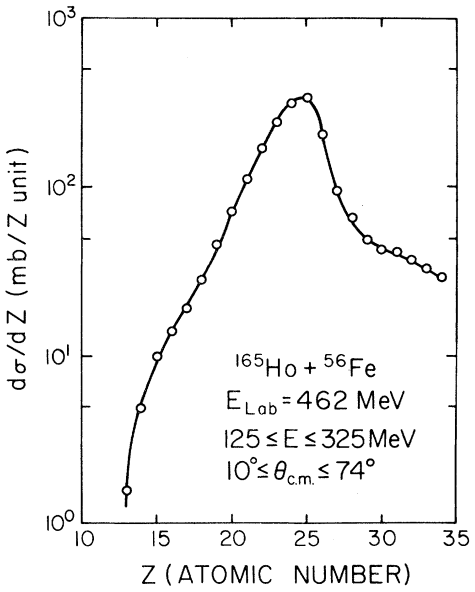

FIG. 4. The Z distribution for the projectilelike fragments integrated over the indicated angle and total kinetic energy ranges.

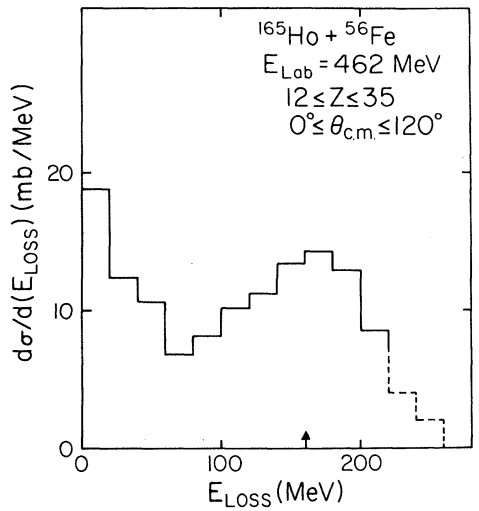

FIG. 5. The energy loss distribution for the damped events integrated over angle in the range $0° \leq \theta_{c.m.} \leq 120°$. The dashed portion represents a region where the cross section was estimated to be 100 mb (see text). The arrow indicates the available kinetic energy E_0 in the entrance channel, i.e., $E_0 = E_{c.m.} - V_C(R_{SA})$.

C. Correlations of experimental observables with fragment charge and energy loss

The distribution of the double differential cross section with respect to final kinetic energy E and fragment Z is shown in Fig. 6 in terms of a contour plot, integrated over all angles. Starting from the iron projectile $Z=26$, the cross section develops a ridge decreasing in Z and broadening as kinetic energy is dissipated. Also observable is a small peak centered close to $Z \approx 46.5$, where fusion-fission fragments are expected. Its centroid deviates slightly from the value expected for symmetric fission of the composite nucleus. This discrepancy is probably due to uncertainties in the Z calibration in this region. The total kinetic energy of the fusion-fission fragments is observed to be about 175 MeV, a value predicted by the systematics of Viola.[15] The width of the fission fragment Z distribution is subject to the same large uncertainties in the Z calibration mentioned above. The dashed curve represents the values of the Coulomb barrier V_C of spheres touching at a separation equal to the strong-absorption radius R_{SA} for different fragmentations.

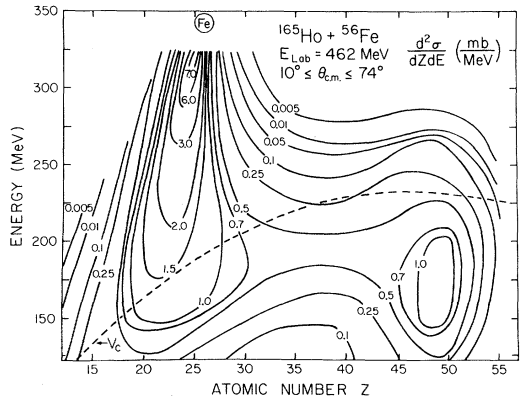

FIG. 6. Contour plot of total kinetic energy vs Z integrated over angle. Full lines are given in units of $d^2\sigma/dZ\,dE$. The dashed line represents the Coulomb barrier V_C for touching spheres for different fragmentations.

In order to examine the relationship between the charge distribution and the final kinetic energy, the differential cross section $d^2\sigma/dZ\,dE$ is plotted in Fig. 7 as a function of Z for 20 MeV wide kinetic energy bins. The distributions become increasingly broader with energy loss, a feature typical of damped reactions and suggestive of a statistical nucleon exchange process evolving in time while collective energy is dissipated. In order to determine the moments, Gaussians were fitted to the damped Z distributions indicated by the curves in Fig. 7(a). In these fits, more weight was given to the low-Z side of the curves because of possible contamination of the distributions by the fusion-fission events at higher Z values. The centroids $\langle Z_L \rangle$ and variances $\sigma_Z{}^2$ of the Z distributions are given by the circles in Figs. 8 and 9, respectively, as a function of energy loss. A summary of the experimental values for the centroids and variances of the distributions is given in Table II.

In Fig. 8 the centroid of the Z distribution, given by circles, is observed to decrease with increasing energy loss. Two processes may be responsible for this Z drift, depending on the extent to which the observed fragments reflect the primary charge distributions. First, a net transfer of protons to the holmiumlike fragment could explain the direction of the drift. Such behavior is expected from the total binding energy of the system, which favors a more asymmetric distribution of protons between the two interacting nuclei. Second, charged-particle evaporation from the ironlike fragment would produce an apparent drift of the average Z value of the light fragment, especially for higher energy losses. In Sec. IV the second possibility is further explored by means of evaporation calculations.

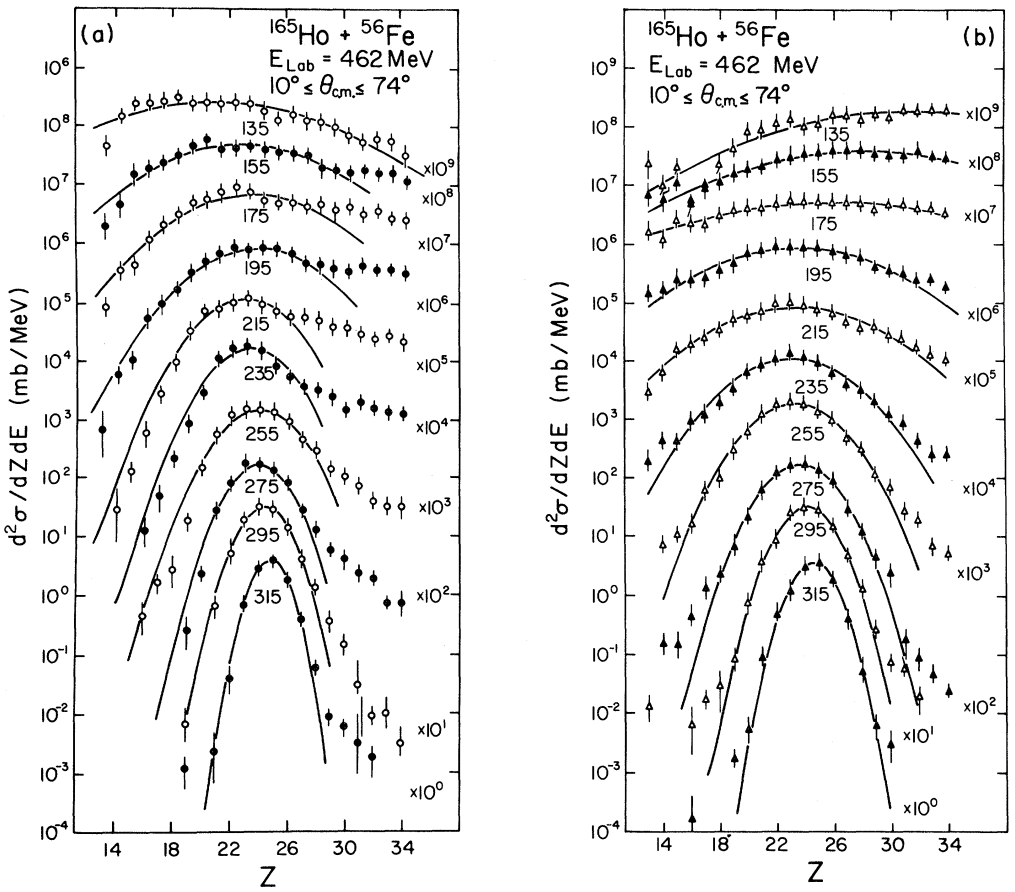

FIG. 7. Fragment Z distributions plotted as a function of total kinetic energy E. Distributions in (a) were made according to the standard analysis procedure; in (b) the modified procedure was used (see text). Energy bins indicated at the maximum of each curve are 20 MeV wide. The curves are displaced by the corresponding factor of 10 listed at the right of each plot. Gaussian fits to the data are indicated by the solid lines.

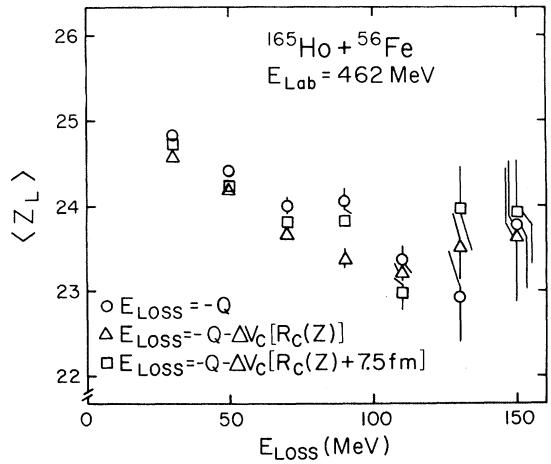

FIG. 8. The centroid of the charge distribution as a function of energy loss is given using the standard (circles) and modified (triangles and squares) procedures. The latter differ in the size of the Coulomb radius (see text).

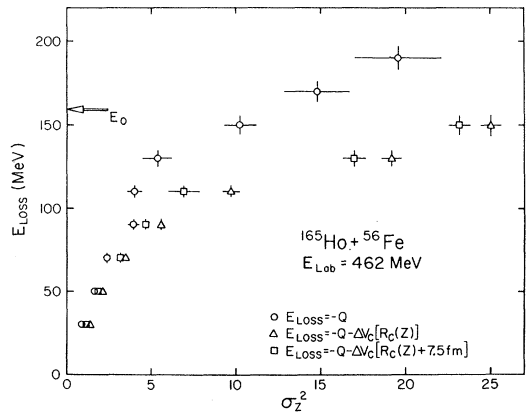

FIG. 9. Experimental correlation between the total kinetic energy loss E_{loss} and the variance $\sigma_Z{}^2$ of the fragment Z distribution using the standard and modified analysis procedures.

TABLE II. ^{165}Ho+^{56}Fe at E_{lab}=462 MeV. The energy windows are 20 MeV wide. The variance $\sigma_Z{}^2$ is corrected for the experimental Z resolution and contains no corrections for the Coulomb barrier. The total cross section accounted for amounts to 2.17 b (quasielastic events and $E_{loss}>210$ MeV are not included). $\bar{\theta}$ is the angle where $d\sigma/d\Omega_{c.m.}$ has its maximum in the c.m. system.

Bin No.	$\langle E \rangle$ (MeV)	$\langle E_{loss} \rangle$ (MeV)	$\sigma_Z{}^2$	$\langle Z_L \rangle$	$d\sigma/dE$ (mb/MeV)	$\bar{\theta}$ (deg)
10	315	30	0.9±0.1	24.8±0.1	12.4	38.0±0.5
9	295	50	1.6±0.2	24.4±0.1	10.6	35.0±0.8
8	275	70	2.4±0.2	24.0±0.1	6.9	31.5±1.0
7	255	90	3.9±0.4	24.1±0.2	8.1	27.5±1.5
6	235	110	4.0±0.4	23.4±0.2	10.1	23.0±2.5
5	215	130	5.4±0.8	22.9±0.6	11.2	16.5±5.0
4	195	150	10.3±1.0	23.8±0.8	13.4	6 ±5
3	175	170	15 ±2	23.4±1.0	14.3	−11 ±5
2	155	190	20 ±3	23 ±1	12.9	−48 ±2
1	135	210	36 ±10	21 ±1	8.6	

The above correlations were derived with respect to kinetic energy loss or reaction Q value, hereafter referred to as the standard analysis procedure. Several authors[16–19] have proposed to consider similar correlations with respect to the loss of kinetic energy above the Coulomb barrier or the sum of Coulomb and centrifugal barriers. Although a physical justification is not indicated for such a procedure, it is interesting that it leads in some cases to more Gaussian-type charge distributions exhibiting an average drift toward a more symmetric fragmentation. In the following discussion this method of analysis will be referred to as the modified procedure.

In a procedure similar to that of Ref. 19, the Z distributions for bins of constant total kinetic energy TKE* were determined, where TKE* = TKE $+ \Delta V_C$, and ΔV_C is the difference between the Coulomb potentials for the exit and entrance channels, evaluated for a configuration of touching spherical nuclei with a center to center distance equal to the strong-absorption radius calculated for each observed mass fragmentation. The modified Z distributions are given in Fig. 7(b). The strong-absorption radius was chosen to calculate the Coulomb energy in order to demonstrate the difference between the two methods of data analysis. Intermediate results were also obtained using Coulomb energies calculated with a radius approximating the distance the fragments would be separated at the highest energy loss measured, corresponding to an increase in distance of 7.5 fm. The Z distributions obtained with the above modified procedure tend to be wider than those corresponding to cuts in the energy loss or Q value, as can be expected from Fig. 6. Plotted in Figs. 8 and 9 are the centroids $\langle Z_L \rangle$ and variances $\sigma_Z{}^2$, respectively, of Gaussian fits to the fragment charge distributions, deduced with Coulomb energies evaluated at separation distances of $r=R_{SA}$ (triangles) and $r=R_{SA}+7.5$ fm (squares).

Except for the highest energy losses where the widths and centroids are poorly defined, certain differences in the Z distributions resulting from the two procedures are apparent. For energy losses less than 150 MeV, the modified procedure yields average fragment Z values lower than those resulting from the standard method. At higher energy losses, the modified analysis results in a more symmetric fragmentation and wider distributions than the latter, depending upon the choice of radius. However, a direct comparison of the data evaluated with the two methods may only be valid at the smallest energy losses where both procedures yield Gaussian distributions. Data obtained with the standard analysis procedure appear narrower at high energy losses because of constraints in the fit procedure. In the modified procedure, the separation distance chosen for evaluating the Coulomb energy has a strong influence on the width of the distributions. Of similar consequence is the inclusion of the centrifugal energies in such considerations.

The variation of the energy spectra with the fragment Z may be viewed as an indicator of a possible constraint in the transfer of charge im-

posed by changes in the Coulomb energies.[6] In Fig. 10 the double differential cross section with respect to Z and total kinetic energy is plotted as a step histogram versus total kinetic energy for various fragment Z values. The events were sorted into bins of three Z units in width, with the centroids given in the figure. The Coulomb energy for spheres separated by the strong-absorption radius R_{SA} for each fragment pair is indicated by an arrow. The different curves are dominated by the

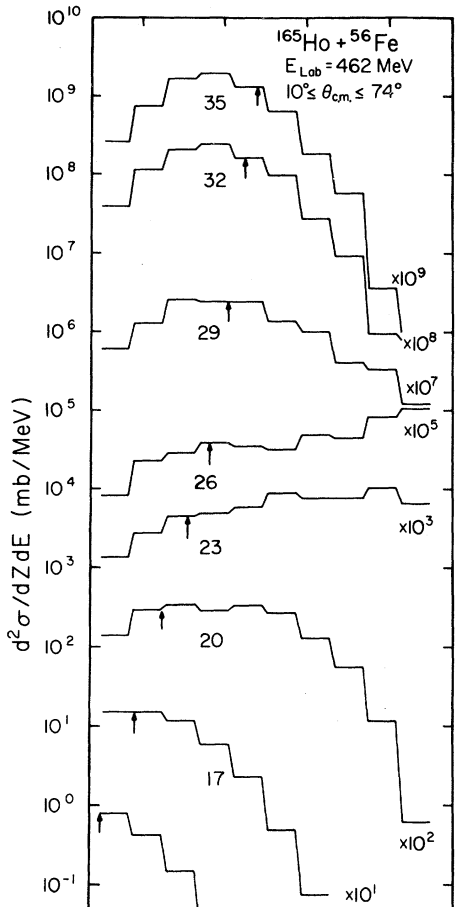

FIG. 10. Double differential cross section $d^2\sigma/dZ\,dE$ vs total kinetic energy is plotted as a function of fragment Z for three Z unit wide bins. The horizontal bars indicate an energy bin of 20 MeV. In the center of each curve is marked the midpoint of the corresponding bin in Z. The arrows represent the Coulomb energies for spherical fragments.

low energy loss events near the projectile Z and large energy loss events for Z values away from the projectile.

Strong correlations between the magnitude of the Coulomb energy and the position of the damped energy peak would indicate significant constraints on the charge transfer process. However, in Fig. 10 such strong correlations are not observed. Although the validity of modification of the analysis to account for a change in the Coulomb energy cannot be ruled out, the data provide no evidence for a significant Coulomb constraint on charge transfer processes. There is also no convincing physical basis for excluding certain parts of the total collective energy from the balance between available and dissipated energies. Data presented in the following sections were obtained from the standard analysis technique, interpreting the total kinetic energy loss or reaction Q value as an essential observable characterizing the progress of the reaction.

D. Correlations dependent upon scattering angle

The angular distribution of the projectilelike damped fragments is plotted in Fig. 11 as $d^2\sigma/d\theta_{c.m.}dE$ versus angle for 20 MeV wide energy bins. The full curves represent fits to be discussed in Sec. IV. Sorting these data with reference to a final kinetic energy parameter, accounting for a variation of the Coulomb barrier as described in Sec. III C, produces no significant change in the shape or width of the angular distributions. At low energy losses the data show a pronounced peak near the quarter-point angle $\theta_{1/4}$(c.m.)=43°, approaching a constant value of $d^2\sigma/d\theta_{c.m.}dE$ which is equivalent to a $1/\sin\theta$ dependence for $d^2\sigma/d\Omega\,dE$ at the higher energy losses.

The narrow angular distributions observed for small energy losses are characteristic of short interaction times. As energy is dissipated, broader angular distributions result, suggesting a steady increase of the interaction time with energy loss.

The progress of the reaction can be deduced from Fig. 12, where a contour diagram (Wilczyński plot) of the double differential cross section for damped events is shown, plotted versus total kinetic energy E and the reaction angle $\theta_{c.m.}$. A pronounced cross section ridge is observed, which extends from the grazing angle at high final energies and moves to lower energies for smaller angles. A second ridge merges with it at forward angles, de-

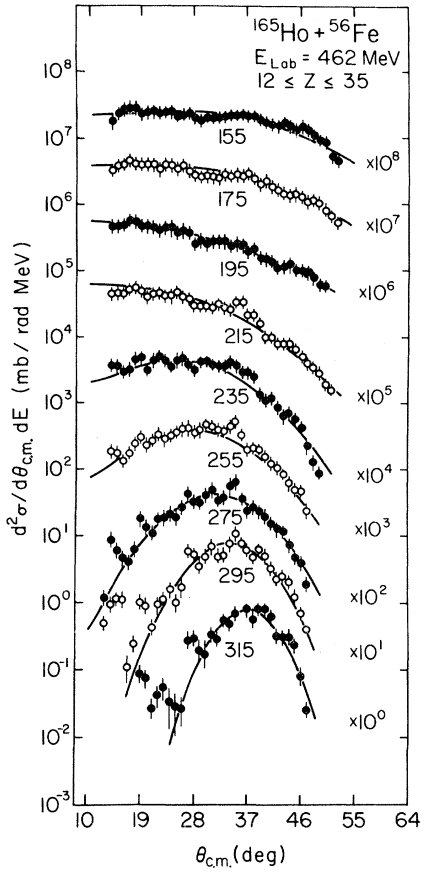

FIG. 11. Angular distributions plotted as the double differential cross sections $d^2\sigma/d\theta_{c.m.}dE$ vs scattering angle, as a function of total kinetic energy. The energy bins are 20 MeV wide. The data are integrated over all damped fragment charges, excluding fusion-fission. The solid curves represent fitted curves (see text).

creasing in energy with increasing angle. The positions of the two cross section ridges are indicated by dashed curves in Fig. 12. The trend of the data may be explained either by orbiting[20] or by double rainbow scattering[21,22] processes. Although the form of the deflection function would be different at small impact parameters, both interpretations could conceivably yield enhanced cross section at forward angles, depending in the latter case on the position of the nuclear rainbow angle. In the present data analysis, orbiting is assumed. Evidence for the occurrence of negative-angle scattering was seen by Trautmann *et al.*[23] in measurements of the circular polarization of deexcitation γ rays for the ^{nat}Ag + ^{40}Ar system. This work[23] could not, however, rule out the possibility of contributions from both processes to the low-energy ridge.

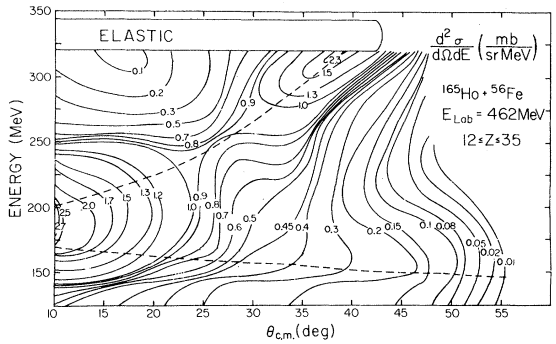

FIG. 12. Double differential cross section $d^2\sigma/d\Omega\,dE$ plotted as a contour diagram (Wilczyński plot) in the total kinetic energy vs scattering angle plane.

In Fig. 13 are shown results of Gaussian fits to fragment Z distributions for different scattering angles and various final energies. The error bars take account of the non-Gaussian shapes of some of the distributions. Although the width (FWHM) of the charge distribution increases with decreasing final kinetic energy, it is nearly independent of angle for a given energy bin. Hence, the reaction angle is not a relevant parameter to describe the evolution of this reaction, an observation in accordance with results reported[1] for other systems.

E. Fusion-fission processes

The angular distribution for fusion-fission events is shown in Fig. 14 as $d\sigma/d\theta_{c.m.}$ versus $\theta_{c.m.}$.

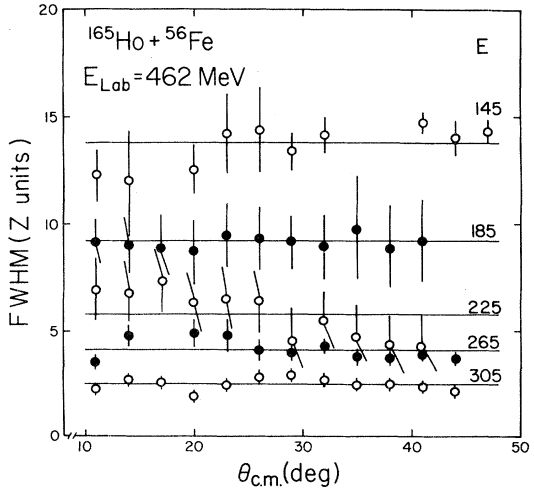

FIG. 13. Widths of Z distribution vs angle shown for five energy bins, 40 MeV wide. The horizontal lines are the average widths for each energy window.

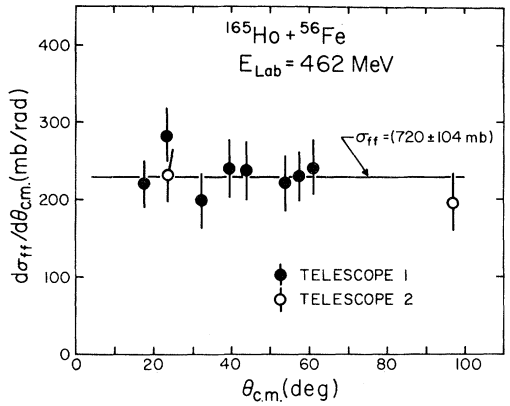

FIG. 14. Differential cross section $d\sigma_{ff}/d\theta_{\text{c.m.}}$ vs angle for fusion-fission events.

These events were identified in the laboratory ΔE-E spectra and transformed into the center-of-mass reference frame assuming a symmetric mass split of the composite system with final total kinetic energies given by the systematics of Viola.[15] The error bars reflect statistical uncertainties and errors associated with the separation of the fusion-fission events from damped events in the ΔE-E spectra.

The data displayed in Fig. 14 are consistent with a $1/\sin\theta_{\text{c.m.}}$ angular dependence, indicated by the horizontal line in the figure. Assuming a constant differential cross section $d\sigma/d\theta_{\text{c.m.}}$ for these events, integration over solid angle yields a cross section $\sigma_{ff}=(720\pm104)$ mb for the fusion-fission-like processes in this reaction, corresponding to $l_{\text{crit}}=125\hbar$. This l value is far in excess of the angular momentum limit ($l_{\text{RLDM}}=66\hbar$) for fission of the compound system as predicted by the rotating liquid drop model.[24]

In accordance with earlier observations,[25] this result suggests the existence of long-lived intermediate systems trapped with high angular momenta in the internuclear potential. These trapped systems, although ultimately unstable, have interaction times sufficiently long to allow considerable relaxation of even slowly equilibrating degrees of freedom, such as the mass asymmetry. Because of the long interaction times, the fragments resulting from these trapped systems exhibit a $1/\sin\theta_{\text{c.m.}}$ angular distribution and have masses and kinetic energies essentially consistent with a fusion-fission reaction process.

IV. PHENOMENOLOGICAL INTERPRETATION OF RESULTS

A. Experimental and theoretical deflection functions

While contour plots such as in Fig. 12 are of interest in describing the progress of a reaction in terms of macroscopic variables, it is sometimes instructive to look at the mean values of these quantities in the form of a deflection function $\theta(l_i)$. In such a diagram an average deflection angle $\bar{\theta}$ is plotted as a function of initial orbital angular momentum l_i or impact parameter.

In order to infer an angular momentum scale from the data, the assumption is made that a monotonic relationship exists between the total kinetic energy loss and the impact parameter. By applying a procedure described in Ref. 26, it is possible to deduce a relation between angular momentum and energy loss by identifying the differential cross section $d\sigma/dE$ corresponding to an energy bin with that associated with an angular momentum window $d\sigma/dl_i$, where

$$\frac{d\sigma}{dl_i}=\pi\lambda\!\!\!^{-2}(2l_i+1)T_{l_i}\ . \tag{4.1}$$

Here, the transmission coefficients T_l can be determined from a sharp cutoff model or from an optical model fit to the elastic scattering angular distribution. In the present case, both techniques were used in order to obtain a better estimate of the uncertainties associated with the conversion. Two normalization points are known: the l value corresponding to the onset of fusion-fission, l_{crit}, and the l value associated with zero energy loss, l_{max}. Results of the conversion are given in the first three columns of Table III.

Plotted in Fig. 15 is the average experimental deflection function for this reaction. The hatched band illustrates the range of derived values associated with different assumptions made in the cross section-to-angular momentum conversion. The angles were determined from the positon of the maximum of the cross section for each particular kinetic energy loss. In this system, because of the substantial amount of orbiting, it was possible to determine accurately the cross section maxima for the highest and lowest energy losses only. Angles for intermediate energies were determined from a smooth interpolation between these limits indicated by the dashed curves in Fig. 12.

The experimental deflection function $\bar{\theta}(l_i)$ is typ-

TABLE III. Results of angular momentum decomposition for nonsticking (NS) and sticking (S) cases.

Bin No.	$\langle E_{loss} \rangle$ (MeV)	$\langle l_i \rangle$ ($\hbar$)	t_{int}^{NS} ($\times 10^{-22}$ sec)	$\langle l_f \rangle^S$ ($\hbar$)	t_{int}^{S} ($\times 10^{-22}$ sec)
10	30	214±8	1.3±0.4	122±5	3.6±0.6
9	50	206±10	1.8±0.4	118±5	4.7±1.0
8	70	200±10	2.5±0.6	114±6	6.0±1.2
7	90	193±10	3.1±0.6	111±5	7.3±1.2
6	110	186±11	4.2±0.9	106±6	9.2±1.6
5	130	177±11	5.7±1.2	101±6	11.9±2.3
4	150	165±11	8.0±1.8	94±6	16.5±3.5
3	170	150±13	12.3±2.9	86±7	24.2±5.2
2	190	130±16	21.9±4.9	74±9	41.5±10.5
1	210				

ical of those for lighter systems, with a Coulomb rainbow angle near l_{max}. In this region of high impact parameters quasielastic events are observed, with deflection angles determined mainly by the long-range part of the interaction potential. The low impact parameter collisions probe the potential at smaller separation distances and are also more strongly influenced by the repulsive Coulomb potential. Since the deflection function reflects the gross features of the potential and friction, it is interesting to compare the experimental deflection function with model calculations.

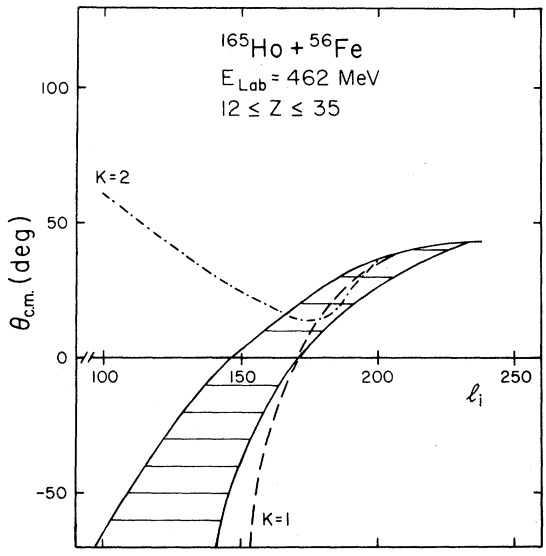

FIG. 15. Experimental deflection function indicated by the solid lines is compared to classical trajectory calculations using the standard $\kappa=2$ (dot-dashed line) and modified $\kappa=1$ (dashed line) proximity potentials.

Results are shown in Fig. 15 for classical trajectory model calculations using nuclear proximity potentials corresponding to different ratios κ by which the nuclear matter distribution of the combined system is allowed to exceed the equilibrium bulk density. The model involves two spherical nuclei in a a frozen configuration and considers four degrees of freedom: the radial separation distance and the orientation angles of the system and its two constituents. It is a simplified version of the model discussed in Sec. V, and is described in detail in Ref. 27.

The dotted-dashed curve in Fig. 15 is based on the interaction potential of Bløcki *et al.*,[28] which is calculated with the assumption of frozen nuclear densities, i.e., $\kappa=2$. The potential with $\kappa=2$ is seen to lead to disagreement between theoretical and experimental deflection functions for $l_i < 150\hbar$. In order to obtain better agreement with the data, it is necessary to relax the sudden-interaction or frozen-density idealization. The dashed curve is calculated from a modified proximity potential[29] corresponding to the situation where no excess nuclear density ($\kappa=1$) is allowed. This potential represents the adiabatic limit and is attractive for all distances. The proximity potential with $\kappa=1$ results in a deflection function which is in reasonable agreement with the experimental deflection function for the damped reaction events.

From the slope of the deflection function, the angular distributions shown in Fig. 11 can be analyzed using a theory developed by Strutinsky,[30,31] where the cross section is divided into coherent and fluctuating contributions. The method was first used to describe quasielastic and transfer reactions, but has subsequently been ex-

tended to damped reactions by Aleschin[32] and Hartmann[33] and applied to the $^{166}Er + {}^{86}Kr$ reaction by Rudolf *et al.*[34] In this method the observed width of the angular distributions shown in Fig. 11 is analyzed in terms of quantal and dynamical angular dispersions associated with l waves of a window around the central value l_0. Statistical fluctuations which may also contribute to the total width of the angular distribution are not further considered in the simplified model discussed below, although they are included in a more sophisticated version of the Strutinsky model.[35]

The form of the angular distributions associated with coherent processes is predicted to be essentially a sum of two Gaussians centered at θ_0, where $\theta_0=\theta(l_0)$ is the deflection angle corresponding to the average l value in the window:

$$\frac{d^2\sigma}{d\theta\, dE} \propto \exp\left[-\left[\frac{\theta-\theta_o}{\xi}\right]^2\right] + \exp\left[-\left[\frac{\theta+\theta_0}{\xi}\right]^2\right]. \tag{4.2}$$

The quantity ξ is related to the variance σ_θ^2 of the distributions and is equal to $(2\sigma_\theta^2)^{1/2}$. The full widths $\Gamma_\theta=[8(\ln 2)\sigma_\theta^2]^{1/2}$ and the angle differences $\theta_{1/4}-\theta_0$, obtained from fits to the experimental data, represented by the curves in Fig. 11, follow a linear relationship, agreeing closely with the $^{166}Er + {}^{86}Kr$ results[34] for energy losses up to 110 MeV. Above this value, the shapes and widths of the distributions depend on the extent to which the fusion-fission events are included in the analysis. The values of θ_0 resulting from the fits reproduce (within 1°–2°) the maximum $\bar{\theta}$ of the angular distributions for each energy loss, i.e., the experimental deflection function.

The angular dispersion ξ is interpreted as the sum of two terms:

$$\xi=\left[\frac{2}{\Delta^2}+\frac{1}{2}\left[\frac{d\theta}{dl}\right]^2\Delta^2\right]^{1/2}, \tag{4.3}$$

where ξ and $d\theta/dl$ are expressed in radians. The first contribution is associated with quantal fluctuations and the second reflects the dynamical dispersion, dependent on the slope $d\theta/dl$ of the deflection function. In this equation Δ is the width of the l window. For the reaction considered here the quantal dispersion is negligible at all energy losses. By solving for Δ, extimates for the widths of the l window are obtained for six energy bins, yielding an average value $\bar{\Delta}=27\pm9$ for the energy loss range of 30 to 130 MeV. This quantity is comparable to the value determined[33] for the $^{232}Th + {}^{40}Ar$ reaction, $\Delta\approx20$, which was also found to be independent of energy loss. Although it appears necessary to perform a more consistent analysis in terms of Sturtinsky's model, including stochastic contributions to the cross section, before definite conclusions can be reached, it is emphasized that the present results may be taken as an indication that the damped reaction angular distribution is dominantly determined by the dynamical rather than the quantum statistical effects.

B. Angular momentum dependent interaction times

In understanding the various reaction processes it is important to evaluate the respective time scales over which they evolve. Because it is not possible to measure such interaction times directly from the experimental observables, they can only be deduced indirectly by employing a model.

A classical phenomenological reaction model was used to deduce the interaction times as described in Refs. 1, 6, and 26. In this model the projectile is assumed to approach the target nucleus on a Coulomb trajectory up to the Rutherford distance of closest approach or the distance given by the strong-absorption radius R_{SA}, whichever is largest. Then the intermediate system, having dissipated its radial kinetic energy, rotates under the influence of the nuclear interaction through an angle $\Delta\theta$, which is determined from the difference between the experimental reaction angle and the calculated Coulomb deflection function angle.[6,36] The system breaks apart at a separation distance consistent with the measured final kinetic energy. The interaction time $t_{\rm int}(l)$ is then calculated from the following relation:

$$t_{\rm int}(l)=\frac{\Delta\theta(l)\mathscr{I}}{\hbar l_f}, \tag{4.4}$$

where $\mathscr{I}=\mu R_{SA}{}^2$ is the moment of inertia for the orbital motion and μ is the reduced mass of the system. The final orbital angular momentum l_f was evaluated for two limiting cases. Initially, the two fragments are sliding on one another while friction forces cause a reduction of the angular momentum from its initial value l_i. Neglecting the reduction in l, the "nonsticking limit" is characterized by $l_f=l_i$. Later in the reaction the rolling friction leads to further transformation of the orbital angular momentum into intrinsic spins of the

two fragments until the system rotates in a rigid "sticking" condition. The final orbital angular momentum in this limit is determined by

$$l_f = l_i \frac{\mathcal{I}}{\mathcal{I}_S} . \tag{4.5}$$

Here, the rigid body moment of inertia of the total system $\mathcal{I}_S$ is

$$\mathcal{I}_S = \mu R_{SA}^2 + \tfrac{2}{5}(M_P R_P^2 + M_T R_T^2) , \tag{4.6}$$

where M_P, M_T and R_P, R_T are the masses and radii of the projectile and target, respectively.

The resulting interaction times for the nonsticking and sticking cases are plotted versus initial angular momentum in Fig. 16 and collected in Table III. Also indicated in the figure are other characteristic times for this reaction. The long dashed line indicates the interaction times resulting from the classical trajectory model calculations described in Sec. IV A. The modified (κ=1) and standard (κ=2) proximity potentials produce essentially the same interaction times for the region of angular momenta contributing to damped processed in this reaction. It is expected that grazing collisions would be characterized by a nonsticking situation, whereas highly damped collisions would be closer to the sticking limit, as corroborated by γ-multiplicity studies.[37] Although the trajectory calculations do not reproduce this trend, the resulting interaction times agree qualitatively with the times derived in the simple phenomenological analysis described above.

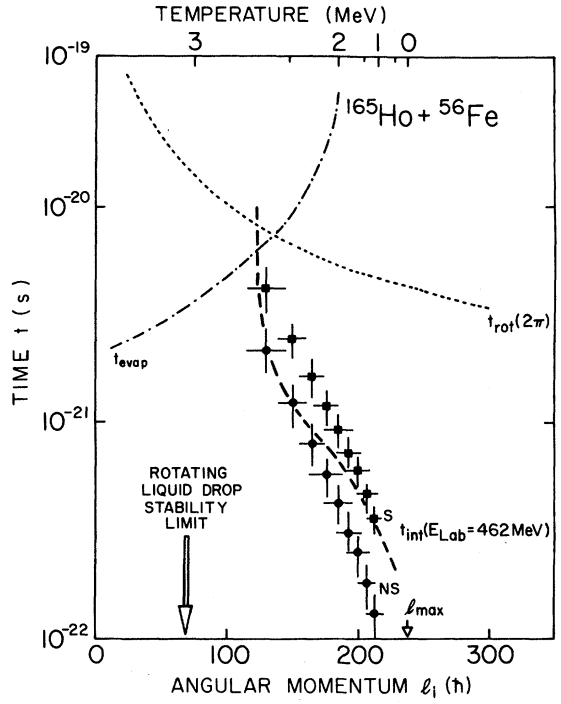

FIG. 16. Characteristic times for the ^{165}Ho + ^{56}Fe reaction plotted as a function of incident angular momentum, or temperature. Experimentally deduced interaction times t_{int} for the sticking (squares) and nonsticking (circles) cases are compared to classical trajectory model calculations (long dashed line). The short dashed line signifies the time for the system to rotate through an angle of 2π and the dotted-dashed line represents the time required for particle evaporation.

The average times t_{evap} for particle evaporation from a compound nucleus have been estimated[38] to be

$$t_{evap} \approx 5 \times 10^{-23} \exp(13 \text{ MeV}/\tau) \text{ sec} , \tag{4.7}$$

where τ is the nuclear temperature. From neutron evaporation measurements[2] for the ^{165}Ho + ^{56}Fe reaction, a relationship between energy loss and nuclear temperature has been derived. Using this information, it was possible to relate the temperature to angular momentum. Typical temperatures observed in the reaction were between 2 and 3 MeV. From a comparison of the relevant time scales depicted in Fig. 16, it is then expected that for the range of l values between 130$\hbar$ and 220$\hbar$, equilibrium particle evaporation must occur after the intermediate system has separated and after the reaction fragments have undergone final acceleration in their mutual Coulomb field. Particle emission from the intermediate system, if observed, would indicate preequilibrium processes in the conventional sense.[39,40] Such a distinction between different emission processes would no longer exist for fusion-fission reactions, where interaction and evaporation times are of similar magnitude.

As suggested by dynamical calculations,[27] the interpenetration of the two reaction partners for small impact parameters may be deep enough and interaction times sufficiently long to achieve partial or complete relaxation of the mass-asymmetry degree of freedom and to ascertain rotation through a significant fraction of a revolution, or more. Lifetimes of the intermediate system formed in these reactions may well be long enough to allow, with a certain probability, for evaporation of light particles prior to separation of the system. Evidence[41] for neutron emission preceding fission has been obtained for the ^{165}Ho + ^{20}Ne reaction at a laboratory energy of 292 MeV.

In principle, the fusion-fission events with $l > l_{RLDM}$ may differ from the compound nucleus fusion-fission events ($l \leq l_{RLDM}$) by having anom-

alous angular and mass distributions. Currently, there is no convincing evidence that mass distribution measurements provide a sensitive method for distinguishing the two conceptually different fusion-fission processes.[42] The angular distribution of fission fragments appears to be a more sensitive method to investigate whether fusion-fission is occurring from deformations inside or outside the unconditional (Bohr-Wheeler) saddle-point shape.[42,43]

V. MICROSCOPIC INTERPRETATION

A. Model description

Although phenomenological trajectory models are useful in describing average reaction properties of damped collisions, a microscopic framework is needed to study the stochastic processes leading to nucleon exchange and the dissipation of energy in a reaction. In the following a dynamical reaction model will be employed to follow explicitly the time evolution of the reaction in terms of the transport of mass, charge, energy, and angular momentum and to obtain predictions to be compared with the data.

Theories based on the one-body interactions of nucleons with the mean nuclear field appear to be applicable to reactions characterized by long mean free paths[44] and low nuclear temperatures. Randrup[29,45] has considered transport phenomena in damped reactions induced by the exchange of individual nucleons between the collision partners, taking proper account of the Pauli exclusion principle.

This approach describes the dynamical evolution of the probability distribution $P(N,Z;t)$ for finding N neutrons and Z protons at time t in the projectilelike fragment in terms of a two dimensional Fokker-Planck equation,

$$\frac{\partial}{\partial t}P=-\left[\frac{\partial}{\partial N}V_N-\frac{\partial}{\partial Z}V_Z+\frac{\partial^2}{\partial N^2}D_N+\frac{\partial^2}{\partial Z^2}D_Z+2\frac{\partial^2}{\partial N\partial Z}D_{NZ}\right]P\ , \quad (5.1)$$

following the work of Nörenberg.[46] The drift and diffusion coefficients V and D determine the first and second moments of the mass and charge distributions and are calculated in Randrup's[29,45] microscopic model. In this model, the mixed diffusion coefficient D_{NZ} is equal to zero. The coefficients have the form

$$V=N'F\ ,$$
$$D=N'\tau^*\ , \quad (5.2)$$

where N' represents the bulk differential current of nucleons with energies near the Fermi surface, as calculated with a Thomas-Fermi approach. The driving force F, governing mass and charge transport, is determined mainly by the gradient of the potential energy surface. The effective temperature τ^* denotes the energy intervals around the Fermi surface that contribute to nucleon exchange. Whereas in a classical diffusion model, the diffusion coefficient is proportional to the nuclear temperature τ, a quantum-statistical approach has to include Pauli blocking which excludes from participation in the diffusion process those single-particle orbits that correspond to the overlap of the Fermi momentum spheres of the two interacting nuclei. This overlap is dependent both on the temperature and the relative velocity. The behavior of τ and τ^* with energy loss is shown in Fig. 17 for this reaction. Early in the reaction, where there is comparatively little overlap of the two Fermi momentum spheres, which are displaced because of the relative velocity, the Pauli blocking is less effective and relatively many levels are available for nucleon exchange, resulting in large values of τ^*. At higher energy losses, where the relative velocity is small, Pauli blocking is more effective and τ^* decreases, eventually approaching the nuclear temperature τ.

Following Swiatecki,[47] a reaction model was developed which approximates the dinuclear configuration by two spheres connected by a small

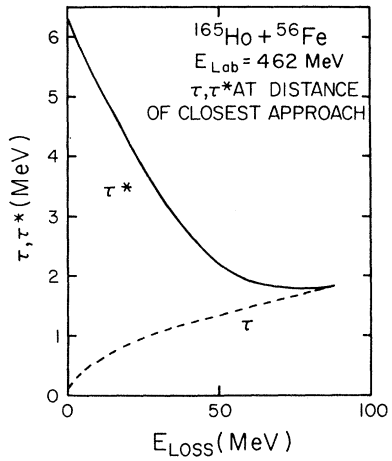

FIG. 17. The thermodynamic and effective nuclear temperatures, τ and τ^*, respectively, plotted vs energy loss (see text).

cylindrical neck. The configuration is pictured schematically in Fig. 18. The seven degrees of freedom in the calculations include the separation distance r between the two centers, the orientation θ of the total system, the angles θ_P and θ_T specifying the orientation of the projectilelike and targetlike fragments, respectively, the neck radius ρ, and the mass A_P and charge Z_P of the projectilelike fragment. Apart from a choice of the interaction potential, the model does not require any arbitrary adjustment of parameters.

In this geometry, the minimum distance s between the two nuclei is expressed as

$$s=r-C_T-C_P\ , \tag{5.3}$$

where C_T and C_P are the matter half density radii of the target and projectile, respectively. The neck length d is approximated by

$$d\approx s+\frac{\rho^2}{2\bar{R}}\ , \tag{5.4}$$

where the reduced radius is defined as

$$\bar{R}=\frac{C_TC_P}{C_T+C_P}\ . \tag{5.5}$$

In order to account for the diffuseness of the nuclear surfaces, an effective neck length $d_{\rm eff}$ is given by

$$d_{\rm eff}=d-s_{\rm crit}\left[1-\frac{\rho}{2\bar{R}}\right]\ . \tag{5.6}$$

The quantity $s_{\rm crit}=-b\Phi(0)\approx 1.8$ fm represents the minimum (geometrical) neck length defined by the proximity force function[45] Φ and the surface width[48] $b=1$ fm.

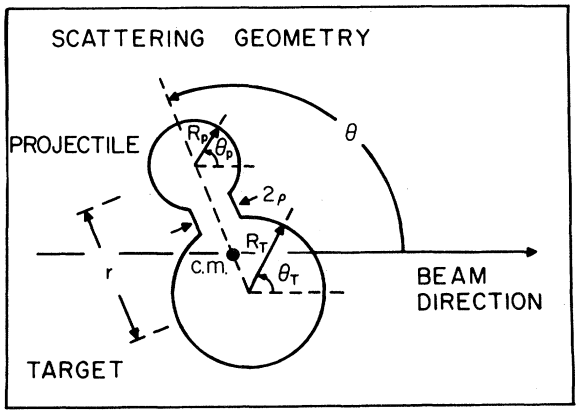

FIG. 18. Scattering geometry for the dynamical reaction model as described in the text.

Dynamical calculations[49] were performed yielding mean trajectories in a multidimensional coordinate space by solving the Lagrange-Rayleigh equations of motion for this system along the coordinates q_i:

$$\left[\frac{d}{dt}\frac{\partial}{\partial\dot{q}_i}-\frac{\partial}{\partial q_i}\right]L=-\frac{\partial}{\partial\dot{q}_i}F,\quad q_i\epsilon\{r,\theta,\theta_p,\theta_T\}\ , \tag{5.7}$$

$$\frac{\partial}{\partial q_i}L=\frac{\partial}{\partial\dot{q}_i}F,\quad q_i\epsilon\{\rho,A_P,Z_P\}\ . \tag{5.8}$$

Here, $L=T-V$ is the Lagrangian and F denotes the dissipation function.

The total interaction potential V accounts for the liquid drop surface energy of the configuration, the nuclear proximity interaction between surfaces outside the neck region, the Coulomb potential calculated according to Bondorf *et al.*,[50] and changes in the nuclear binding energies derived from the droplet model,[51] including shell corrections. The nuclear potential[47] is given by

$$V_{\rm nucl}=-2\pi\gamma\rho^2+2\pi\gamma\rho d_{\rm eff}+4\pi\gamma\bar{R}b\Phi(d/b)\exp(-\rho^2/2\bar{R}b)\ , \tag{5.9}$$

where $\gamma=1$ MeV/fm^2 is the surface tension. The first term describes the surface energy of the two caps erased by the presence of the neck and the second term is the energy of the neck surface formed. The third term contains the remaining proximity interaction of the opposing nuclear surfaces outside the neck. At small separations the resulting nuclear potential is somewhat shallower than the modified proximity potential[29] discussed in Sec. IV because of the added energy required to form the neck surface.

The dissipation function F contains terms arising from the relative motion, the neck motion, and changes in the average mass and charge asymmetries. The friction force acting on the relative motion is assumed to be due to the recoil induced by nucleons passing through a transparent window between the collision partners as described by the "window formula."[47] This term is given by

$$F_{\rm rel}=2\pi n_0\bar{R}b\tilde{\Psi}(\rho,s)(u_\perp{}^2+\tfrac{1}{2}u_{||}{}^2)\ , \tag{5.10}$$

where $n_0=2.63\times10^{-23}$ MeV sec fm^{-4} is the bulk energy flux in nuclear matter and $u_\perp$ and $u_{||}$ represent the velocity components perpendicular and parallel to the interface area between the two collision partners, respectively. The transmission function

$$\tilde{\Psi}(\rho,s)=\frac{\rho^2}{2\bar{R}b}+\Psi\left[\frac{d}{b}\right]e^{-\rho^2/2\bar{R}b} \tag{5.11}$$

measures the transparency of the effective window which includes the fully open part inside the neck. In the above equation, Ψ is the proximity flux function. The damping of the neck motion arises from collisions of nucleons with its walls ("wall formula").[47] This motion is assumed to be overdamped and the corresponding dissipation function is given by

$$F_{\text{neck}}=4\pi n_0\rho d e^{-d/(\rho+b)}\dot{\rho}^2 . \tag{5.12}$$

Reactions at low bombarding energies such as that studied here are expected to be strongly influenced by the features of the appropriate multidimensional potential energy surface. Figure 19 shows contour lines of potential energy surfaces calculated from a rotating liquid drop model including shell corrections, plotted versus neutron number N_1 and atomic number Z_1 for one of the fragments. The potential contains the sum of the fragment binding energies, the Coulomb, nuclear, and centrifugal potentials, and has the form

$$V(Z_1,N_1)=V_{LD}(Z_1,N_1)+V_{LD}(Z_2,N_2)+V_{\text{Coul}}(Z_1,Z_2,r)+V_{\text{nucl}}(A_1,A_2,r,\rho)+\frac{\hbar^2 l^2}{2\mu r^2}-U_0 . \tag{5.13}$$

In the above equation, the constant U_0 is chosen so that the initial fragmentation (denoted by a cross in the figure) is normalized to zero at a separation distance equal to the strong-absorption radius R_{SA}. Figure 19(a), corresponding to $l=0$ and $\rho=0$, shows a surface with an elongated valley defined by steep slopes with a deep minimum at symmetry and a shallower one at the $N=28$ shell. The heavy solid line starting at the initial fragmentation indicates the experimentally observed trajectory using the mean values $\langle Z\rangle$ and $\langle N_1\rangle=\langle A_1\rangle-\langle Z_1\rangle$. The average masses were taken from the mass measurements of Ref. 4. The observed trajectory initially (i.e., for low energy losses or high l values) responds to the gradient of the potential, but may not follow this gradient for higher energy losses. Here, perhaps, uncertainties in the corrections to the data for particle evaporation may also become important.

A more realistic comparison would include the dependence of the potential energy surface on angular momentum and neck parameter. The

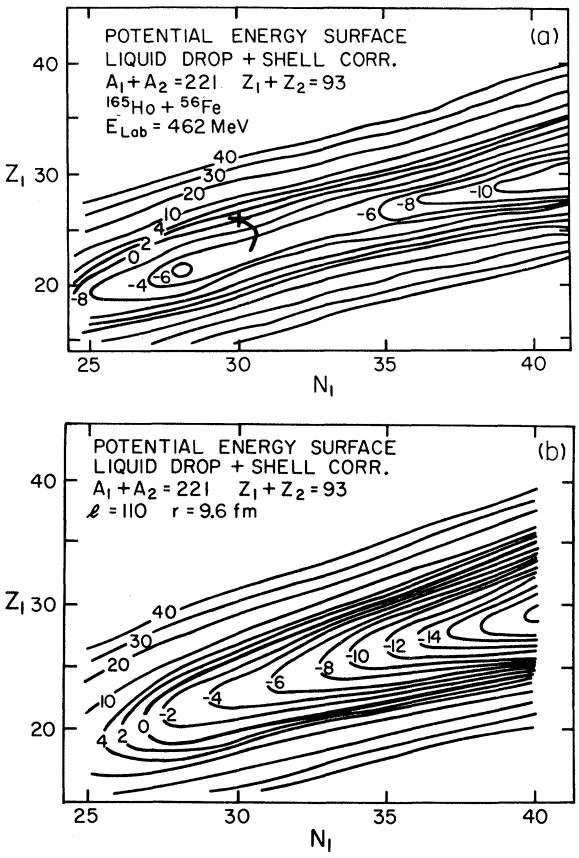

FIG. 19. Potential energy surfaces calculated from the liquid drop model for (a) $l=0$ and (b) $l=110\hbar$ for the compound system. The cross and heavy line signify the injection point and observed trajectory, respectively.

dynamical calculations predict a trajectory with an incident angular momentum $l_i=150\hbar$ to reach a distance of closest approach of 9.6 fm, while the angular momentum is decreased to a value of $110\hbar$. The potential energy surface applicable in this case, where shell effects have become relatively less important, as pictured in Fig. 19(b), looks somewhat different from the $l=0$ surface. The surface suggests a relatively large drift of the mass and charge distribution towards symmetry, in constrast to the observed data. The observation of a large drift in Z would, however, be contingent on whether there is sufficient time to reach such a condition. At present it is not clear how to calculate a more realistic potential energy surface and how to incorporate it into a consistent dynamical reaction model.

The outstanding feature of the dinuclear configurations considered in the reaction model discussed

above is the existence of a cylindrical neck connecting the two spherical nuclei. Since it largely determines the extent to which the two nuclei communicate, the development of the neck during a collision is significant for the outcome of the reaction.

A cut through the total potential energy surface of Eq. (5.13) corresponding to the initial mass and charge asymmetry and $l=0$ is given in Fig. 20(a). The ordinate is a "reduced neck radius," ρ/C_P, where C_P is defined as the matter half density radius of the projectile. For small radii there is a forbidden region determined by the minimum geometrical overlap of the two nuclei at each distance r. The effect of the addition of the centrifugal term in the potential is illustrated in Fig. 20(b), where the potential energy surface for $l_i=200\hbar$ superimposed on the surface is represented by a dashed line.

In the entrance channel the trajectory indicates that the system follows the path of minimum neck size until a turning point is reached. From this point on, the neck stretches and the fragments move apart. Here, the trajectories would be expected to follow the gradient of the corresponding time-dependent effective potential if it were not for the dynamical effects associated with dissipation. With increasing distance between the two fragments, the neck radius decreases monotonically until it snaps at fragment separations several fm larger than where it was first formed in the entrance channel.

In Fig. 21 average trajectories for $l_i = 130\hbar$ and $180\hbar$ are plotted as correlations of dissipated kinetic energy and distance s between the two fragment centers. The dissipated energy E_{diss} is defined as the total kinetic energy loss E_{loss}, neglecting the spin energy. The solid curves were calculated using the nuclear interaction potential of Eq. (5.9). The dashed curves in the figure represent results obtained in calculations referred to in Sec. IV, employing the modified nuclear proximity potential[29] ($\kappa=2$) and the corresponding dissipation function,[29] neglecting the neck degree of freedom. Both trajectories indicate the onset of dissipation when the distance between the two spheres is somewhat less than $s=s_{SA}$, corresponding to a distance between the two nuclei equal to the strong-absorption radius R_{SA}. The trajectories start out similarly because in both cases for surface separations larger than a critical value s_{crit} (≈ 1.8 fm) when the neck is not yet formed, the potential and dissipation functions are determined by the prox-

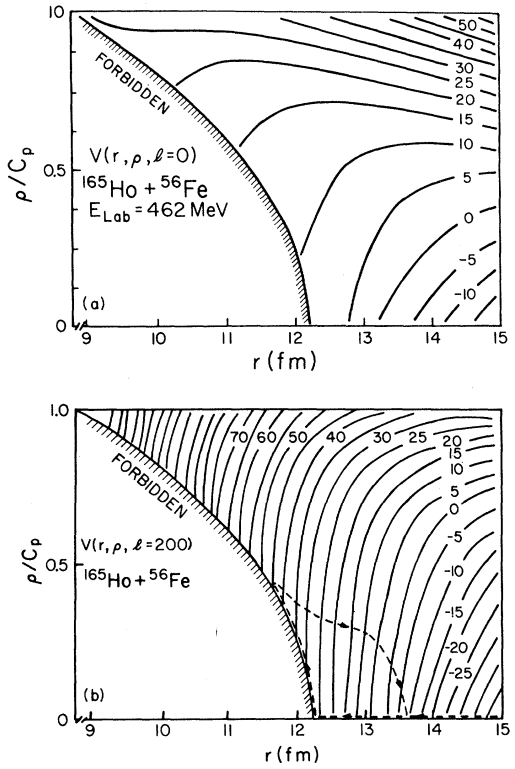

FIG. 20. Potential energy surfaces for $l=0$ and $l=200\hbar$ plotted as reduced neck radius versus distance r. The corresponding trajectory for $l_i=200\hbar$ is superimposed on the surface in (b). The triangular area is inaccessible.

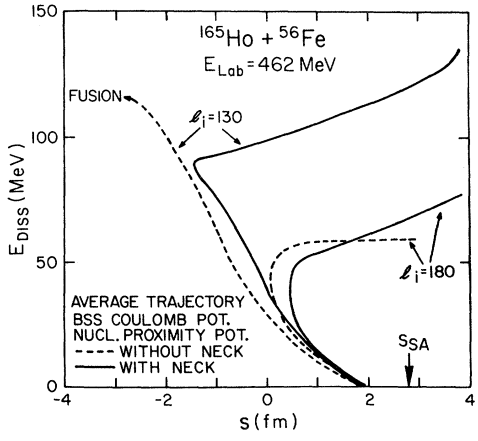

FIG. 21. The average trajectory derived from dynamical calculations is illustrated in a plot of dissipated energy E_{diss} vs the distance s between the two nuclei for $l_i = 130\hbar$ and $180\hbar$. The dashed and solid curves represent calculations with and without the inclusion of the neck degree of freedom, respectively.

imity form factors [cf. Eqs. (5.4)–(5.11)]. Following the $l_i = 130\hbar$ trajectory, corresponding to the proximity treatment neglecting neck effects the two nuclei continue interpenetrating until they fuse. In the model accounting for the neck degree of freedom, an initial angular momentum $l_i = 130\hbar$ does not lead to fusion. In this case, at an overlap of about $s = -1.5$ fm, a turning point is reached where the neck ceases to grow. This reduction of the predicted fusion cross section is expected because the potential of Eq. (5.9) is somewhat shallower than the modified proximity potential. In the exit channel, the neck area shrinks, dissipating energy, until it finally snaps. For $l_i = 180\hbar$, the two trajectories are fairly similar with lesser amounts of interpenetration than the corresponding trajectories for $l_i = 130\hbar$. Here, the additional energy dissipated due to the neck motion is observable in the exit channel.

Although the development of a neck between two interacting nuclei is intuitively expected to occur, this degree of freedom is treated in the model only in a very approximate manner. Its validity for damped nuclear collisions can only be inferred from a comparison to experiment.

B. Comparison to data

Results of model calculations described in the preceding section are compared in Fig. 22 to experimentally deduced interaction times, angle, and energy loss as a function of angular momentum. The interaction times deduced in Sec. IV B for the nonsticking and sticking cases as well as the average experimental deflection function are observed to be in agreement with the calculations, within the experimental errors. As seen from the lower part of the figure, the measured energy loss compares favorably with the model except for the highest energy losses, where presumably large deformations of the system develop that cannot be described by the model. The agreement with the data supports the assumption of a monotonic relationship between E_{loss} and l underlying the phenomenological analysis described in Sec. IV.

In Fig. 23 the model calculations, shown as a dashed curve, are compared to experimental correlations between total kinetic energy and average center-of-mass angle. The data points were deduced from projections of the Wilczyński plot (cf. Fig. 12) to energy and angle axes, where the angle associated with the maximum cross section for each energy bin is plotted in Fig. 23 versus centroid of the bin. Because a significant fraction of the reaction contributes to orbiting, the above procedure to obtain an energy loss-angle relation could not be applied for a range of intermediate energy losses. The solid line in Fig. 23 (equivalent to the dashed curves in Fig. 12) represents an attempt to interpolate the relation in this region of final kinetic energies. As can be observed from a comparison of the dashed curve with the data points in Fig. 23, the theory provides a reasonable description of the data down to final energies close to the Coulomb barrier V_C, where again deviations are expected since large deformations are unaccounted for in the model.

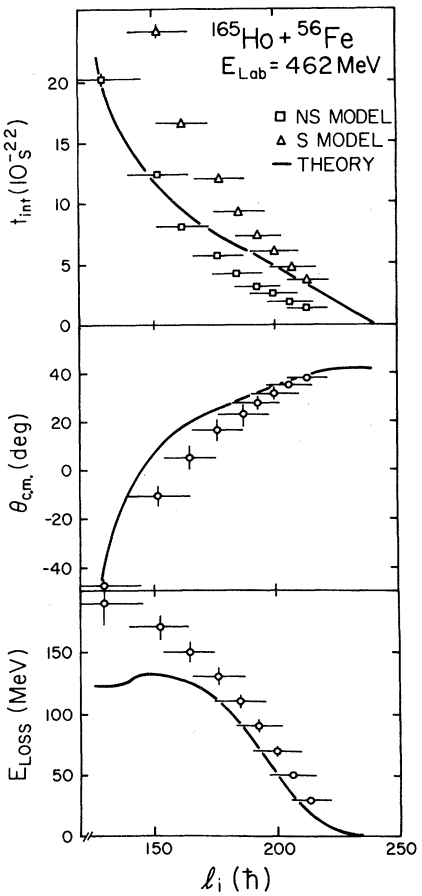

FIG. 22. Derived interaction times for nonsticking and sticking models, scattering angle, and energy loss plotted vs initial angular momentum. The full curves represent results of dynamical calculations.

The measured centroid $\langle Z_L \rangle$ of the Z distributions is plotted in Fig. 24 and compared to model predictions, given by a solid line. The drift in Z seems to agree with the data in direction but not in magnitude. The experimental results should not,

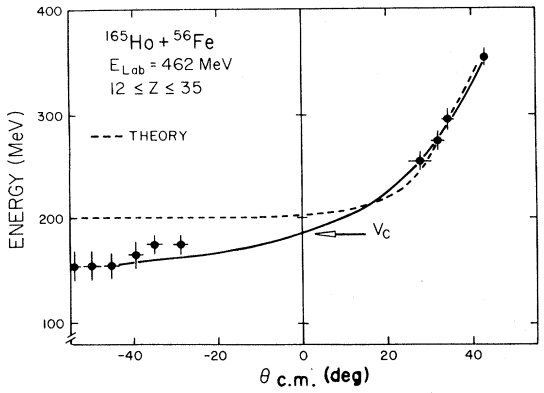

FIG. 23. Total kinetic energy vs angle. The maxima of the cross section is given by the heavy line which represents a smooth interpolation of the experimental data. Model calculations are represented by the dashed line. The Coulomb barrier V_C is noted in the figure.

however, be directly compared to the calculations because of the possible effect of particle evaporation from the primary fragments. Therefore, evaporation calculations were performed for representative light primary fragments at three different excitation energies using the code MBII.[52] The excitation energy of the fragments was related to the average energy loss which was assumed to be divided between the two fragments according to their mass ratio and was corrected for the ground state Q values, Q_{gg}. The intrinsic spin J of the fragments was estimated assuming the sticking limit for two spherical nuclei. In a method described in Ref. 2, the final orbital angular momentum l_f of the system is assumed to be given by the sticking limit for energy losses greater than 130 MeV, corresponding to an initial angular momentum $l_i = 177\hbar$. For higher angular momenta, the ratio $(l_i - l_f) / l_i$ is assumed to decrease linearly to zero as l_i approaches l_{max}. This procedure is based on observations of γ multiplicities in damped reactions reported by Olmi *et al.*,[53] which were interpreted in terms of the theory of angular momentum dissipation of Wolschin and Nörenberg.[54]

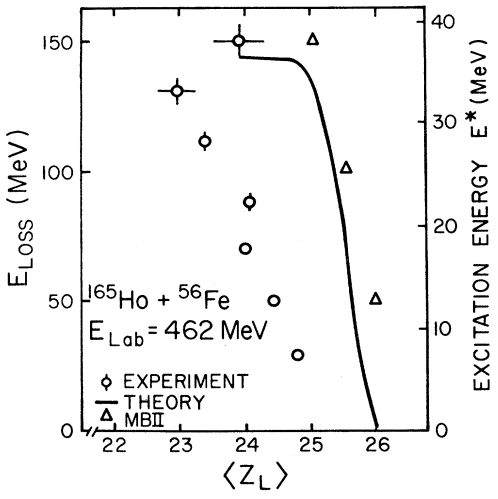

FIG. 24. The centroid of the final Z distributions (circles) plotted as a function of energy loss compared to theoretical calculations (solid line). The triangles are the predicted fragments following charged-particle evaporation from a hypothetical primary fragment ^{56}Fe using the code MBII and plotted vs excitation energy E^*.

In order to illustrate the maximum effect of charged-particle evaporation, the triangles in Fig. 24 indicate the predicted average Z values of the secondary fragments resulting from evaporation from the primary ^{56}Fe fragment at various excitation energies. As indicated in the figure, little or no charged-particle emission is expected for such a primary fragment for energy losses up to 100 MeV, such that the observed Z distributions are tentatively interpreted as representing the primary distribution. If the observed Z distributions are subject to corrections much larger than suggested by these evaporation calculations, better agreement between experiment and model would result. However, definite conclusions must await analysis of experimental results[5] of a measurement of the charged-particle emission in the reaction.

In the model, the variances σ_A^2 and σ_Z^2, of the fragment mass and charge distributions, respectively, are obtained from integrating the transport coefficients along the trajectory. In Fig. 25 the results of the calculations, represented by a solid line, are compared with the data. The calculations reproduce the data fairly well up to energy losses of about 130 MeV. The dashed curve represents dynamical calculations in the classical limit, taking no account of the Pauli exclusion principle in the nucleon exchange processes. The results for this reaction, as well as those described in Ref. 49, indicate that the Pauli principle is essential in order to obtain a description of the data, as can be expected for bombarding energies per nucleon that are low compared to the nucleon Fermi velocity.

The results of evaporation calculations discussed above were used to examine the effect of charged-particle emission on the widths of the Z distributions. The results indicate that there is, in general, only a small influence on the width from particle

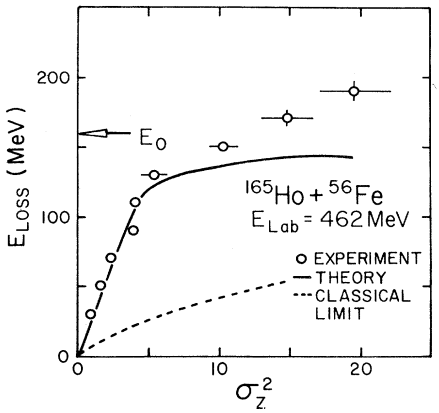

FIG. 25. Experimental variances $\sigma_Z{}^2$ plotted vs energy loss are compared to model predictions (solid curve). The dashed curve is a calculation estimating the classical limit for the reaction.

evaporation for a range of excitation energies of the projectilelike fragments.

VI. CONCLUSIONS

The full range of reaction processes from elastic scattering to fusion-fission reactions has been studied for the $^{165}Ho + ^{56}Fe$ reaction at a beam energy of $E_{lab} = 462$ MeV. Correlations of experimental observables with energy loss are presented for varying degrees of energy damping. The angular distributions show a substantial amount of orbiting to negative angles, demonstrating that the nuclear force remains attractive even at large interpenetrations. The fragment Z distributions are observed to increase steadily in width as the reaction progresses, indicating the importance of nucleon exchange in this reaction.

Classical phenomenological models are used to deduce angular momenta and interaction times for the system. The derived average deflection function decreases to negative angles for intermediate and small l values, similar to those of lighter systems. Interaction times for the damped products range from 10^{-22} to 10^{-21} sec depending upon the energy loss. The more highly damped composite systems which lead to fusion-fission may undergo one or more rotations and possibly have lifetimes sufficiently long to evaporate neutrons and charged particles before breakup.

Dynamical calculations which assume a dinuclear configuration with a cylindrical neck compare favorably with the data on average quantities up to regions where the system is expected to be strongly deformed. Calculated trajectories are used to derive dispersions of fragment charge distributions from theoretical transport coefficients. Satisfactory agreement between predictions and calculations for correlations between charge dispersions and energy loss lend strong support to the dominance of a one-body nucleon exchange mechanism underlying the observed transport phenomena.

ACKNOWLEDGMENTS

This work was supported by the U. S. Department of Energy. The use of the facilities at the Nuclear Structure Research Laboratory was supported by the National Science Foundation. The authors would like to acknowledge the cordial hospitality of LBL and to thank especially H. Grunder, R. Stevenson, and the staff of the Super HILAC for providing an efficient operation of the accelerator. Special recognition is due to M. Zisman for his efficient and conscientious help in the experiments.

*Present address: Lawrence Livermore National Laboratory, University of California, Livermore, California.

†Present address: Hahn-Meitner Institut, Berlin, West Germany.

[1]W. U. Schröder and J. R. Huizenga, Annu. Rev. Nucl. Sci. 27, 465 (1977), and references cited therein.

[2]D. Hilscher, J. R. Birkelund, A. D. Hoover, W. U. Schröder, W. W. Wilcke, J. R. Huizenga, A. C. Mignerey, K. L. Wolf, H. F. Breuer, and V. E. Viola, Jr., Phys. Rev. C 20, 576 (1979).

[3]A. D. Hoover, L. E. Tubbs, J. R. Birkelund, W. W. Wilcke, W. U. Schröder, D. Hilscher, and J. R. Huizenga (unpublished).

[4]H. Breuer, B. G. Glagola, V. E. Viola, K. L. Wolf, A. C. Mignerey, J. R. Birkelund, D. Hilscher, A. D. Hoover, J. R. Huizenga, W. U. Schröder, and W. W. Wilcke, Phys. Rev. Lett. 43, 191 (1979).

[5]W. W. Wilcke, J. R. Birkelund, J. P. Kosky, D. Hilscher, A. D. Hoover, J. R. Huizenga, W. U.

Schröder, and H. J. Wollersheim (unpublished).
[6]W. U. Schröder, J. R. Birkelund, J. R. Huizenga, K. L. Wolf, and V. E. Viola, Jr., Phys. Rep. 45C, 301 (1978).
[7]J. R. Birkelund, J. R. Huizenga, H. Freiesleben, K. L. Wolf, J. P. Unik, and V. E. Viola, Jr., Phys. Rev. C 13, 133 (1976).
[8]L. C. Northcliffe and R. F. Schilling, Nucl. Data, Sect. A 7, 233 (1970).
[9]F. Hubert, A. Fleury, R. Bimbot, and D. Gardes, Ann. Phys. (Paris) Suppl. 5, 1 (1980).
[10]S. B. Kaufman, E. P. Steinberg, B. D. Wilkins, J. Unik, A. J. Gorski, and M. J. Fluss, Nucl. Instrum. Methods 115, 47 (1974).
[11]J. B. Moulton, J. E. Stephenson, R. P. Schmitt, and G. J. Wozniak, Nucl. Instrum. Methods 157, 325 (1978).
[12]F. G. Perey (unpublished).
[13]W. E. Frahn and R. H. Venter, Ann. Phys. (N.Y.) 24, 243 (1963); W. E. Frahn, Phys. Rev. Lett. 26, 568 (1971); Ann. Phys. (N.Y.) 72, 524 (1972).
[14]W. E. Frahn, Nucl. Phys. A302, 267 (1978).
[15]V. E. Viola, Jr., Nucl. Data Sect. A 1, 391 (1966).
[16]L. G. Moretto and R. Schmitt, J. Phys. (Paris) C 5, 109 (1976).
[17]G. Rudolf, A. Gobbi, H. Stelzer, U. Lynen, A. Olmi, H. Sann, R. G. Stokstad, and D. Pelte, Nucl. Phys. A330, 243 (1979).
[18]S. Agarwal, J. Galin, B. Gatty, D. Guerreau, M. Lefort, X. Tarrago, R. Babinet, B. Cauvin, J. Girard, and H. Nifenecker, Nucl. Phys. A293, 230 (1977).
[19]J. S. Sventek and L. G. Moretto, Phys. Rev. Lett. 40, 697 (1978).
[20]J. Wilczyński, Phys. Lett. 47B, 484 (1973).
[21]H. H. Deubler and K. Dietrich, Phys. Lett. 56B, 241 (1975).
[22]D. H. E. Gross and H. Kalinowski, Phys. Lett. 48B, 302 (1974).
[23]W. Trautmann, J. de Boer, W. Dünnweber, G. Graw, R. Kopp, C. Lauterbach, H. Puchta, and U. Lynen, Phys. Rev. Lett. 39, 1062 (1977); W. Trautmann, *Proceedings of the International Symposium on Continuum Spectra of Heavy Ion Reactions, San Antonio, 1979* (Harwood Academic, New York, 1980).
[24]S. Cohen, F. Plasil, and W. J. Swiatecki, Ann. Phys. (N.Y.) 82, 557 (1974).
[25]B. Heusch, C. Volant, H. Freiesleben, R. D. Chestnut, K. D. Hildenbrand, F. Pühlhofer, W. F. W. Schneider, B. Kohlmeyer, and W. Pfeffer, Z. Phys. A 288, 391 (1978).
[26]W. U. Schröder, J. R. Birkelund, J. R. Huizenga, K. L. Wolf, and V. E. Viola, Jr., Phys. Rev. C 16, 623 (1977).
[27]J. R. Birkelund, L. E. Tubbs, J. R. Huizenga, J. N. De, and D. Sperber, Phys. Rep. 56C, 107 (1979).
[28]J. Bløcki, J. Randrup, W. J. Swiatecki, and C. F. Tsang, Ann. Phys. (N.Y.) 105, 427 (1977).
[29]J. Randrup, Nucl. Phys. A307, 319 (1978).
[30]V. M. Strutinsky, Zh. Eksp. Teor. Fiz. 46, 2078 (1964) [Sov. Phys.—JETP 19, 1401 (1964)].
[31]V. M. Strutinsky, Phys. Lett. 44B, 245 (1973).
[32]V. P. Aleshin, Yad. Fiz. 20, 497 (1974) [Sov. J. Nucl. Phys. 20, 267 (1975)].
[33]K. M. Hartmann, Nucl. Phys. A305, 279 (1978).
[34]G. Rudolf, U. Lynen, A. Gobbi, A. Olmi, and H. Sann, Nucl. Phys. A367, 109 (1981).
[35]V. Strutinsky, Z. Phys. A 286, 77 (1978).
[36]J. P. Bondorf, J. R. Huizenga, M. I. Sobel, and D. Sperber, Phys. Rev. C 11, 1265 (1975).
[37]P. Glässel, R. S. Simon, R. M. Diamond, R. C. Jared, I. Y. Lee, L. G. Moretto, J. O. Newton, R. Schmitt, and F. S. Stephens, Phys. Rev. Lett. 38, 331 (1977).
[38]R. G. Stokstad, Proceedings of the Conference on Heavy Ion Collisions, Fall Creek Falls, 1977, Report CONF-770602 (unpublished).
[39]J. J. Griffin, Phys. Rev. Lett. 17, 478 (1966).
[40]M. Blann, Annu. Rev. Nucl. Sci. 25, 123 (1975).
[41]D. Hilscher, E. Holub, U. Jahnke, H. Orf, and H. Rossner, Contribution to the Third Adriatic Europhysics Study Conference on the Dynamics of Heavy-Ion Collisions, Hvar, Yugoslavia, 1981 (unpublished).
[42]J. R. Huizenga, J. R. Birkelund, W. U. Schröder, W. W. Wilcke, and H. J. Wollersheim, Contribution to the Third Adriatic Europhysics Study Conference on the Dynamics of Heavy-Ion Collisions, Hvar, Yugoslavia, 1981 (unpublished).
[43]B. B. Back, H. G. Clerc, R. R. Betts, B. G. Glagola, and B. D. Wilkins, Phys. Rev. Lett. 46, 1068 (1981).
[44]M. T. Collins and J. J. Griffin, University of Maryland Report TR80-041, 1980.
[45]J. Randrup, Nucl. Phys. A327, 490 (1979).
[46]W. Nörenberg, Phys. Lett. 52B, 289 (1974); Z. Phys. A 274, 241 (1975).
[47]W. J. Swiatecki, Lawrence Berkeley Laboratory Report LBL-8950, 1979 (unpublished).
[48]W. D. Myers, Nucl. Phys. A204, 465 (1973).
[49]W. U. Schröder, J. R. Birkelund, J. R. Huizenga, W. W. Wilcke, and J. Randrup, Phys. Rev. Lett. 44, 308 (1980).
[50]J. P. Bondorf, M. I. Sobel, and D. Sperber, Phys. Rep. 15C, 83 (1974).
[51]W. D. Myers, *Droplet Model of Atomic Nuclei* (IFI/Plenum, New York, 1977).
[52]M. Beckerman and M. Blann, University of Rochester Report UR-NSRL-135A, 1977 (unpublished).
[53]A. Olmi, H. Sann. D. Pelte, Y. Eyal, A. Gobbi, W. Kohl, U. Lynen, G. Rudolf, H. Stelzer, and R. Bock, Phys. Rev. Lett. 41, 688 (1978).
[54]G. Wolschin and W. Nörenberg, Phys. Rev. Lett. 41, 691 (1978).